Constraining Non-Methane VOC Emissions with TROPOMI HCHO observations: Impact on Summertime Ozone Simulation in August 2022 in China

Shuzhuang Feng[1], Fei Jiang[1,2,5*], Tianlu Qian[3], Nan Wang[4], Mengwei Jia[1], Songci Zheng[1], Jiansong Chen[6], Fang Ying[6], Weimin Ju[1,2]

[1] *Jiangsu Provincial Key Laboratory of Geographic Information Science and Technology, International Institute for Earth System Science, Nanjing University, Nanjing, 210023, China*

[2] *Jiangsu Center for Collaborative Innovation in Geographical Information Resource Development and Application, Nanjing, 210023, China*

[3] *School of Internet of Things, Nanjing University of Posts and Telecommunications, Nanjing, 210042, China*

[4] *College of Carbon Neutrality Future Technology, Sichuan University, Chengdu, 610207, China*

[5] *Frontiers Science Center for Critical Earth Material Cycling, Nanjing University, Nanjing, 210023, China*

[6] *Hangzhou Municipal Ecology and Environment Bureau, Hangzhou, 310020, China*

* Corresponding author: Tel.: +86-25-83597077; Fax: +86-25-83592288; E-mail address: jiangf@nju.edu.cn

Abstract

Non-methane volatile organic compounds (NMVOC), serving as crucial precursors of O_3, have a significant impact on atmospheric oxidative capacity and O_3 formation. However, both anthropogenic and biogenic NMVOC emissions remain subject to considerable uncertainty. Here, we extended the Regional multi-Air Pollutant Assimilation System (RAPAS) with the EnKF algorithm to optimize NMVOC emissions in China in August 2022 by assimilating TROPOMI HCHO retrievals. We also simultaneously optimize NO_x emissions by assimilating in-situ NO_2 observations to address the chemical feedback among VOC-NO_x-O_3. Furthermore, a process-based analysis was employed to quantify the impact of NMVOC emission changes on various chemical reactions related to O_3 formation and depletion. NMVOC emissions exhibited a substantial reduction of 50.2%, especially in the middle and lower reaches of the Yangtze River, revealing a prior overestimation of biogenic NMVOC emissions due to extreme heatwave. Compared with the forecast with prior NMVOC emissions, the forecast with posterior emissions significantly improved HCHO simulations, reducing biases by 75.7%, indicating a notable decrease in posterior emission uncertainties. The forecast with posterior emissions also effectively corrected the overestimation of O_3 in forecast with prior emissions, reducing biases by 49.3%. This can be primarily attributed to a significant decrease in the RO_2 + NO reaction rate and an increase in the NO_2 + OH reaction rate in the afternoon, thus limiting O_3 generation. Sensitivity analyses emphasized the necessity of considering both NMVOC and NO_x emissions for a comprehensive assessment of O_3 chemistry. This study enhances our understanding of the effects of NMVOC emissions on O_3 production and can contribute to the development of effective emission reduction policies.

Keywords

NMVOC emissions, O_3 pollution, Emission inversion, HCHO column retrievals, Data assimilation

1 Introduction

Since the Chinese government implemented the Air Pollution Prevention and Control Action Plan in 2013, there has been a notable reduction in NO_x emissions (Zheng et al., 2018). However, despite these advancements, the issue of O_3 pollution persists and, in certain cases, has shown signs of worsening (Ren et al., 2022). The increase in O_3 concentration can be attributed not only to adverse meteorological conditions but also predominantly to unbalanced joint control of non-methane volatile organic compounds (NMVOCs) and nitrogen oxides (NO_x) (Li et al., 2020). NMVOCs are vital precursors of O_3 and have a substantial impact on the atmospheric oxidation capacity, thereby altering the lifetimes of other pollutants. Accurately quantifying NMVOC emissions holds significant importance in investigating their impact on O_3 chemistry and in formulating emission reduction policies.

Anthropogenic NMVOC emissions have traditionally been estimated using a "bottom-up" method. However, the accuracy and timeliness of these estimations face challenges owing to the scarcity of local measurements for emission factors, the incompleteness and unreliability of activity data, and the diverse range of species and technologies involved (Cao et al., 2018; Hong et al., 2017). Furthermore, uncertainties arise in model-ready NMVOC emissions due to spatial and temporal allocations using various "proxy" data for different source sectors (Li et al., 2017a). Li et al. (2021) reported substantial discrepancies among emission estimates in various studies, ranging 23% to 56%. Biogenic NMVOC emissions are typically estimated using models like the Model of Emissions of Gases and Aerosols from Nature (MEGAN) (Guenther et al., 2012) and the Biogenic Emission Inventory System (BEIS) (Pierce et al., 1998). NMVOC emissions result from the multiplication of plant-specific standard emission rates by dimensionless activity factors. Nonetheless, apart from inaccuracies in the distribution of plant functional types, empirical parameterization, especially concerning responses to temperature and drought stress, can introduce substantial uncertainties (Angot et al., 2020; Seco et al., 2022; Jiang et al., 2018). Warneke et al. (2010) determined isoprene emission rates through field measurements and conducted a comparison with MEGAN and BEIS estimates, revealing a notable tendency for MEGAN to overestimate emissions, while BEIS consistently underestimated them. Similarly, Marais et al. (2014) found that MEGAN's isoprene emission estimates were 5-10 times higher than the canopy-scale flux measurements obtained from African field campaigns.

A top-down approach, utilizing observed data, has been developed for estimating VOCs emissions. For instance, based on aircraft and ground-based field measurements, the source-receptor relationships algorithm with Lagrangian particle dispersion model (Fang et al., 2016), mixed layer gradient techniques (Mo et al., 2020), eddy covariance flux measurements (Yuan et al., 2015), and box model (Wang et al., 2020) have been employed to complement or verify bottom-up results. However, these approaches do not comprehensively consider the complex nonlinear chemical reactions and transport processes that VOCs undergo in the atmosphere. Formaldehyde (HCHO) and glyoxal (CHOCHO) in the atmosphere serve as crucial oxidization intermediates for various VOCs (Hong et al., 2021; Liu et al., 2012). Satellite-based observations can readily detect their presence in the form of vertical column density (VCD) from space, making them widely utilized for estimating NMVOC emissions. A commonly used approach assumes that the observed HCHO/CHOCHO columns are locally linearly correlated with VOC emission rates (Palmer et al., 2006; Liu et al., 2012). However, this approach does not consider the spatial offset resulting from chemistry reactions and transport processes. Chaliyakunnel et al. (2019) conducted a Bayesian analysis to derive an optimal estimate of VOC emissions using HCHO measurements over the Indian subcontinent. Their results indicated that biogenic VOC emissions modeled by MEGANv2.1 were overestimated by approximately 30–60%, whereas anthropogenic VOC emissions derived from the RETRO inventory were underestimated by 13–16%. Cao et al. (2018) employed the GEOS-Chem model and its adjoint, incorporating tropospheric HCHO and CHOCHO column data from the GOME-2A and OMI satellites as constraints, to quantify Chinese NMVOC emissions. They demonstrated a low bias in the MEGAN model, in contrast to the significant overestimation shown in Bauwens et al. (2016), especially in southern China.

Several investigations have been conducted to explore the implications of inverted VOC emissions on surface O_3. For instance, using the Eulerian box model, Zhou et al. (2023) employed concurrent VOC measurements to constrain anthropogenic VOC emissions. This led to improved simulations of VOCs and O_3, with a reduction in high emissions by 15%–36% in the Pearl River Delta (PRD) region. Local model biases in simulating the oxidation of NMVOCs and O_3 are closed related to uncertainties in NO_x emissions (Wolfe et al., 2016; Chan Miller et al., 2017). To tackle these critical questions, Kaiser et al. (2018) applied an adjoint algorithm to estimate isoprene

emission over the southeast US by downwardly adjusting anthropogenic NO_x emissions by 50% to rectify NO_2 simulations. Their findings indicated that isoprene emissions from MEGAN v2.1 were overestimated by an average of 40%, slightly lower than the 50% reduction in Bauwens et al. (2016). Souri et al. (2020) simultaneously optimized NMVOC and NO_x emissions utilizing OMPS-NM HCHO and OMI NO_2 retrievals in East Asia. They found that predominantly anthropogenic NMVOC emissions from MIX-Asia 2010 increased over the North China Plain (NCP), whereas predominantly biogenic NMVOC emissions from MEGAN v2.1 decreased over southern China after the adjustment. Unfortunately, the posterior simulations exacerbated the overestimation of O_3 levels in northern China.

Most studies regarding the inversion of NMVOC emissions or its impact on O_3 neglected the uncertainties associated with NO_x-dependent production or loss of NMVOC oxidation and O_3. An iteratively nonlinear joint inversion of NO_x and NMVOCs using multi-species observations is expected to minimize the uncertainties in their emissions and is well-suited to address the intricate relationship among VOC-NO_x-O_3. In this study, we extended the Regional multi-Air Pollutant Assimilation System (RAPAS) upon the ensemble Kalman filter (EnKF) assimilation algorithm to enhance the optimization of NMVOC emissions over China, utilizing the TROPOspheric Monitoring Instrument (TROPOMI) HCHO retrievals with high spatial coverage and resolution. To more accurately quantify the impact of NMVOC emissions on O_3, NO_x emissions were simultaneously adjusted using nationwide in-situ NO_2 observations. Process analysis was subsequently employed to quantify various chemical pathways associated with O_3 formation and loss. Through a top-down constraint on both emissions, this study aims to offer a more scientific insight into the consequences of optimizing NMVOC emissions on O_3 and contribute to the development of appropriate emission reduction policies.

2 Data and Methods

2.1 Data Assimilation System

The RAPAS system (Feng et al., 2023) has been developed based on a regional chemical transport model (CTM) and ensemble square root filter (EnSRF) assimilation modules (Whitaker and Hamill, 2002), which are employed for simulating atmospheric compositions and inferring anthropogenic emissions by assimilating surface

observations, respectively (Feng et al., 2022; Feng et al., 2020). The inversion process follows a two-step procedure within each inversion window, in which the emissions are inferred first and then input into the CMAQ model to simulate initial conditions of the next window. Meanwhile, the optimized emissions are transferred to the next window as prior emissions. The two-step inversion strategy facilitates error propagation and iterative emission optimization, which have proven the superiority and robustness of our system in estimating emissions (Feng et al., 2023). In this study, we extended the data frame to include the assimilation of TROPOMI HCHO retrievals for optimizing NMVOC emissions. Concise descriptions of the forecast model, data assimilation approach, and experimental settings follow.

2.1.1 Atmospheric Transport Model

The Weather Research and Forecast (WRF v4.0) model (Skamarock and Klemp, 2008) and the Community Multiscale Air Quality Modeling System (CMAQ v5.0.2) (Byun and Schere, 2006) were applied to simulate meteorological conditions and atmospheric chemistry, respectively. WRF simulations were conducted with a 27-km horizontal resolution, covering the entire mainland China on a grid of 225×165 cells (Figure 1). The CMAQ model was run over the same domain, but with a removal of three grid cells on each side of the WRF domain. The vertical settings in WRF and CMAQ was the same as Feng et al. (2020). To account for the rapid expansion of urbanization, we updated underlying surface information for urban and built-up land using the MODIS Land Cover Type Product (MCD12C1) Version 6.1 of 2022. Chemical lateral boundary conditions for NO, NO_2, HCHO, and O_3 were extracted from the output of the global CTM (i.e., the Whole Atmosphere Community Climate Model, WACCM) with a resolution of $0.9° \times 1.25°$ at 6-hour intervals (Marsh et al., 2013). Meanwhile, boundary conditions for the other NMVOCs were obtained directly from background profiles. In the first data assimilation (DA) window, chemical initial conditions (excluding NMVOCs) were also derived from the WACCM outputs, whereas in subsequent windows, they were derived through forward simulation using optimized emissions from the previous window. Table S1 lists the detailed physical and chemical configurations. To assess the impact of updated NMVOC emissions on O_3 production efficiency, we further decoupled the contribution of the primary chemical processes to the O_3 levels using the CMAQ Integrated Reaction Rate (IRR) analysis.

2.1.2 EnKF Assimilation Algorithm

The emissions are constrained using the Ensemble Square Root Filter (EnSRF) algorithm introduced by Whitaker and Hamill (2002). This approach fully accounts for temporal and geographical variations in both the transportation and chemical reactions within the emission estimates. During the forecast step, the background ensembles are derived by applying perturbation to the prior emissions. The perturbed samples are typically drawn from Gaussian distributions with a mean of zero and a standard deviation equal to the prior emission uncertainty in each grid cell. Ensemble runs of the CMAQ model were subsequently performed to propagate the background errors with each ensemble sample of state vectors.

In the analysis step, the ensemble mean $\overline{X^a}$ of the analyzed state is regarded as the best estimate of emissions, which is obtained by updating the background ensemble mean through the following equations:

$$\overline{X^a} = \overline{X^b} + \mathbf{K}(\mathbf{y} - H\overline{X^b}) \tag{1}$$

$$\mathbf{K} = \boldsymbol{P^b}\boldsymbol{H}^T(\boldsymbol{H}\boldsymbol{P^b}\boldsymbol{H}^T + \boldsymbol{R})^{-1} \tag{2}$$

where $\boldsymbol{y}$ is the observational vector; $\boldsymbol{H}$ represents the observation operator mapping model space to observation space; The expression $\boldsymbol{y} - \boldsymbol{H}\overline{X^b}$ quantifies the disparities between simulated and observed concentrations; $\boldsymbol{P^b}\boldsymbol{H}^T$ illustrates how uncertainties in emissions relate to uncertainties in simulated concentrations; The Kalman gain matrix $\boldsymbol{K}$, dependent on background error covariance $\boldsymbol{P^b}$ and observation error covariance $\boldsymbol{R}$, determines the relative contributions to the updated analysis.

State variables for emissions include NO_x and NMVOCs. To reduce the degree of freedom in the analysis and avoid the difficulty associated with estimating spatio-temporal variations in background errors for individual species, we focus on optimizing the lumped total NMVOC emissions. During the forecast step, we differentiate individual NMVOC species emissions from the total NMVOC emissions using bottom-up statistical information. For a consistent comparison between simulations and observations, model-simulated NO_2 were diagnosed at the time and location of surface NO_2 measurements, whereas model-simulated HCHO was horizontally sampled to align with TROPOMI HCHO VCD retrievals, and subsequently integrated vertically.

In this study, the DA window was set to one day and daily TROPOMI HCHO columns were utilized as observational constraints in our inversion framework. The ensemble size was set to 50 to strike a balance between computational cost and inversion accuracy. To reduce the impact of unrealistic long-distance error correlations, the Gaspari and Cohn function (Gaspari and Cohn, 1999) was utilized as covariance localization to ensure the meaningful influence of observations on state variables within a specified cutoff radius, while mitigating their negative impacts on distant state variables. The optimal localization scale is interconnected with factors such as the assimilation window, the dynamic system, and the lifetime of chemical species. Given the average wind speed of 2.8 m/s (Table S2) and a DA window of 1 day, the localization scales for NO_2 and HCHO, both characterized as highly reactive species with lifespans of just a few hours, were set to 150 km and 100 km, respectively.

2.2 Observation Data and Errors

Considering the availability of HCHO data, we utilized daily offline retrievals of tropospheric HCHO columns from Sentinel-5P (S5P) L3 TROPOMI data obtained through Google Earth Engine (De Smedt et al., 2018). The S5P satellite follows a near-polar sun-synchronous orbit at an altitude of 824 km with a 17-day repeating cycle. It crosses the Equator at 13:30 local solar time (LST) on the ascending node. The spatial resolution at nadir was refined to $3.5 \times 5.5\,km^2$ on 6 August 2019. Following the recommendations in the S5P HCHO product user manual, we filtered the source data to exclude pixels with qa_value less than 0.5 for HCHO column number density and 0.8 for aerosol index (AER_AI). The remaining high-quality pixels with minimal snow/ice or cloud interference are averaged to 27-km grids. Figure 1b illustrates the coverage and data amount of TROPOMI HCHO retrievals in August 2022 after processing. Although the distribution of filtered data exhibits spatial non-uniformity, most grid cells have observational coverage for over half of the time, particularly in the southern region of China where NMVOC emissions are higher. Based on validation against a global network of 25 ground-based Fourier transform infrared (FTIR) column measurements (Vigouroux et al., 2020), TROPOMI HCHO overestimates by 25% ($<2.5\times10^{15}$ molec cm^{-2}) in clean regions and underestimates by 30% ($>=8\times10^{15}$ molec cm^{-2}) in polluted regions. Therefore, we set the measurement error to 30%. To evaluate the effect of observational data retrieval errors on emission estimates, we conducted a sensitivity experiment in which HCHO columns were empirically bias-corrected

according to the error characteristics described above (Figure S1). The posterior emissions increased by 12.8% compared to those in the base experiment (EMDA), indicating that the existing retrieval error in HCHO measurements likely exerts an influence on the estimation of NMVOC emissions. The representation error can be disregarded because the model's resolution significantly surpasses that of the TROPOMI pixels.

To address the chemical feedback among VOC-NO$_x$-O$_3$, we also simultaneously optimized NO$_x$ emissions by assimilating in-situ NO$_2$ observations. The extensively covered and high-precision monitoring network can provide sufficient constraints for emission inversion (Figure 1a). Hourly averaged surface NO$_2$ observations from national control air quality stations obtained from the Ministry of Ecology and Environment of the People's Republic of China (http://106.37.208.228:8082/, last access: 5 May 2023). In case where multiple stations are located within the same grid, a random site is chosen for validation, while the remaining sites are averaged to mitigate the impact of error correlation (Houtekamer and Zhang, 2016) for assimilation. In total, 1276 stations were chosen for assimilation and an additional 425 independent stations were selected for verification (Figure 1a). The observation error covariance matrix $\boldsymbol{R}$ incorporates contributions from both measurement and representation errors. The measurement error is defined as $\varepsilon_0 = 1.0 + 0.005 \times \Pi_0$, where Π_0 represents the observed NO$_2$ concentration. Following the approach of Elbern et al. (2007) and Feng et al. (2018), the representative error is defined as $\varepsilon_r = \gamma \varepsilon_0 \sqrt{\Delta l / L}$, where γ is a tunable parameter (here, γ=0.5), Δl is the grid spacing (27 km), and L is the radius (here, L=0.5) of the observation's influence area. The total observation error (r) was defined as $r = \sqrt{\varepsilon_0^2 + \varepsilon_r^2}$. The observation errors are assumed to be uncorrelated so that $\boldsymbol{R}$ is a diagonal matrix.
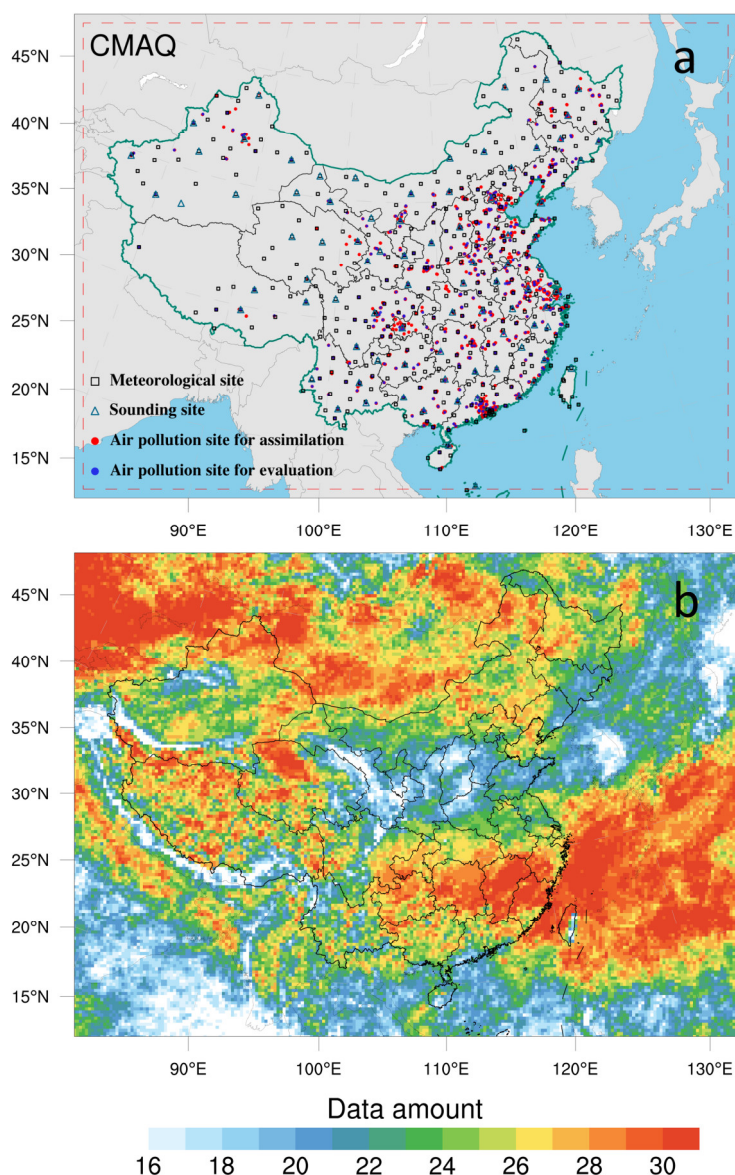
Figure 1. Model domain and observation network (a) and data amount of TROPOMI HCHO retrievals during August 2022 in each grid (b). The red dashed frame delineates the CMAQ computational domain; black squares denote surface meteorological measurement sites; navy triangles indicate sounding sites (Text S1), and red and blue dots represent air pollution measurement sites, where red dots are used for assimilation and blue dots for independent evaluation.

2.3 Prior Emissions and Uncertainties

The prior anthropogenic NO_x and NMVOC emissions for China were obtained from the most recent Multi-resolution Emission Inventory for China of 2020 (MEIC, http://www.meicmodel.org/, last access: 8 May 2023) (Zhang et al., 2009). For anthropogenic emissions outside China, we utilized the mosaic Asian anthropogenic

emission inventory (MIX) for the base year of 2010 (Li et al., 2017b). The daily emission inventory, which was arithmetically averaged from the combined monthly emission inventory, was employed as the first guess. Ship emissions were derived from the shipping emission inventory model (SEIM) for 2017, which was calculated based on the observed vessel automatic identification system (Liu et al., 2017). Biomass burning emissions were retrieved from the Global Fire Emissions Database version 4.1 (GFEDv4, https://www.globalfiredata.org/, last access: 8 May 2023) (van der Werf et al., 2017; Mu et al., 2011). Biogenic NO_x and NMVOC emissions were calculated using the Model of Emissions of Gases and Aerosols from Nature (MEGAN) developed by Guenther et al. (2012).

As previously mentioned, the optimized emissions are transferred to the next DA window as prior emissions for iterative inversion. For biogenic emissions, it is decomposed into hourly scales based on the daily varying temporal profiles in MEGAN as model inputs. Daily emission variations will largely dominate the uncertainty in emissions. Taking into account compensating for model errors and avoiding filter divergence, we consistently applied an uncertainty of 25% to each model grid of NO_x emissions at each DA window, as in Feng et al. (2020). NMVOC emissions typically exhibit greater uncertainties compared to NO_x emissions (Li et al., 2017b). Based on model evaluation, the uncertainty of NMVOC emissions was set to 40% (Kaiser et al., 2018; Souri et al., 2020; Cao et al., 2018). A sensitivity experiment involving a doubling of the prior uncertainty (80%) revealed that the differences in posterior NMVOC emissions amounted to a mere 0.2% (Figure S2). The implementation of a 'two-step' inversion strategy allows for the timely correction of residual errors from the previous assimilation window in the current window, thus ensuring that the RAPAS system has a relatively low dependence on prior uncertainty settings. This study also addresses uncertainties in emissions for CO, SO_2, primary $PM_{2.5}$, and coarse PM_{10} to consider the chemical feedback between different species following Feng et al. (2023).

3 Experimental Design

During the summer of 2022, southern China experienced severe heatwave conditions. The combination of high temperatures and drought had a pronounced effect on vegetation growth and NMVOC emissions, thereby influencing O_3 production (Wang et al., 2023). Consequently, we opted to focus on August 2022, as it presented an ideal period for testing the capabilities of our DA system. Before implementing the emission

inversion, a relatively perfect initial field is generated at 0000 UTC on August 1 2022 through conducting a 5-day simulation with 6-hour interval 3D-Var data assimilation. Subsequently, daily emissions are continuously updated over the entire month of August (EMDA). Additionally, we designed a sensitivity experiment (EMS) to illustrate the significance of optimizing NO_x emissions in quantifying VOC-O_3 chemical reactions. In this experiment, NO_x emissions were not optimized. To validate the posterior emissions of NO_x and NMVOCs in EMDA, we compared two parallel forward simulation experiments, denoted as CEP and VEP, corresponding to prior and posterior emission scenarios, respectively, against NO_2 and HCHO measurements. To investigate the impact of optimizing NMVOC emissions on the secondary production and loss of surface O_3, a forward simulation experiment (CEP1) was conducted with the prior NMVOC emissions and the posterior NO_x emissions. Another forward modelling experiment (CEP2) used the posterior emissions of EMS to evaluate its performance. All experiments employ identical meteorological fields, as well as the same gas-phase and aerosol modules. Table 1 summarizes the different emission inversion and validation experiments conducted in this study.

Table 1. The assimilation, sensitivity, and validation experiments conducted in this study.

Exp.Type	Exp. Name	NMVOC emissions	NO_x emissions
Assimilation	EMDA	MEIC 2020 and MEGAN for August (the first DA window), optimized emissions of the previous window (other DA windows)	MEIC 2020 and MEGAN for August (the first DA window), optimized emissions of the previous window (other DA windows)
Sensitivity	EMS	Same as EMDA	MEIC 2020 and MEGAN for August
Validation	CEP	MEIC 2020 and MEGAN for August	MEIC 2020 and MEGAN for August
	VEP	Posterior emissions of EMDA	Posterior emissions of EMDA
	CEP1	Same as CEP	Posterior emissions of EMDA
	CEP2	Posterior emissions of EMS	Same as CEP

4 Results

4.1 Inverted Emissions

Figure 2 shows the spatial distribution of temporally averaged prior and posterior NMVOC emissions, along with their differences, in NMVOC emissions. Hotspots of prior NMVOC emissions were prevalent across much of central and southern China. However, posterior NMVOC emissions were predominantly concentrated in the NCP, Yangtze River Delta (YRD), PRD, and Sichuan Basin (SCB), characterized by high levels of anthropogenic activity. High emissions are also located in parts of central and southern China with warm climate favorable for emitting biogenic NMVOCs. Employing TROPOMI HCHO observations as constraints led to widespread decreases of approximately 60–70% over these areas, indicating a large substantial of biogenic NMVOC emissions. In northwestern China, there was a moderate increase in NMVOC emissions.

A potential significant TROPOMI retrieval errors in polluted regions could exacerbate the emission decreases (Text S2). Additionally, uncertainties in MEGAN parameterization have significant implications for NMVOC emission estimations, particularly concerning the responses of vegetation in MEGAN to temperature and drought stress (Angot et al., 2020; Jiang et al., 2018). Zhang et al. (2021) highlighted that the temperature-dependent activity factor noticeably increases with rising temperatures in MEGAN. Wang et al. (2021b) pointed out that the missing of a drought scheme is one of the factors causing the overestimation of isoprene emissions in MEGAN. Opacka et al. (2022) optimized the empirical parameter in the MEGANv2.1 soil moisture stress algorithm, resulting in significant reductions in isoprene emissions and providing better agreement between modelled and observed HCHO temporal variability in the central U.S. During the study period, China experienced severe heatwave conditions, which may further hinder the MEGAN's ability to effectively capture the impacts of high temperatures and drought on vegetation, thus resulting in significant overestimation in NMVOC emissions (Wang et al., 2022). Ultimately, the biogenic NMVOC emissions decreased by 53.7%, which was higher than the 43.4% decrease in anthropogenic NMVOC emissions (Figure S3). Overall, the large magnitude of emission decrease of 50.2% in our inversion is comparable to studies in southern China (Bauwens et al., 2016; Zhou et al., 2023), southeastern US (Kaiser et al., 2018), Africa (Marais et al., 2014), India (Chaliyakunnel et al., 2019), Amazonia

(Bauwens et al., 2016), and parts of Europe (Curci et al., 2010), but opposite to the large-scale emission increase over China in Cao et al. (2018). For NO$_x$ (Figure S4), the nationwide total emissions decreased by 10.2%, with the main reductions concentrated in the NCP, YRD, parts of Central China, and most key urban areas.
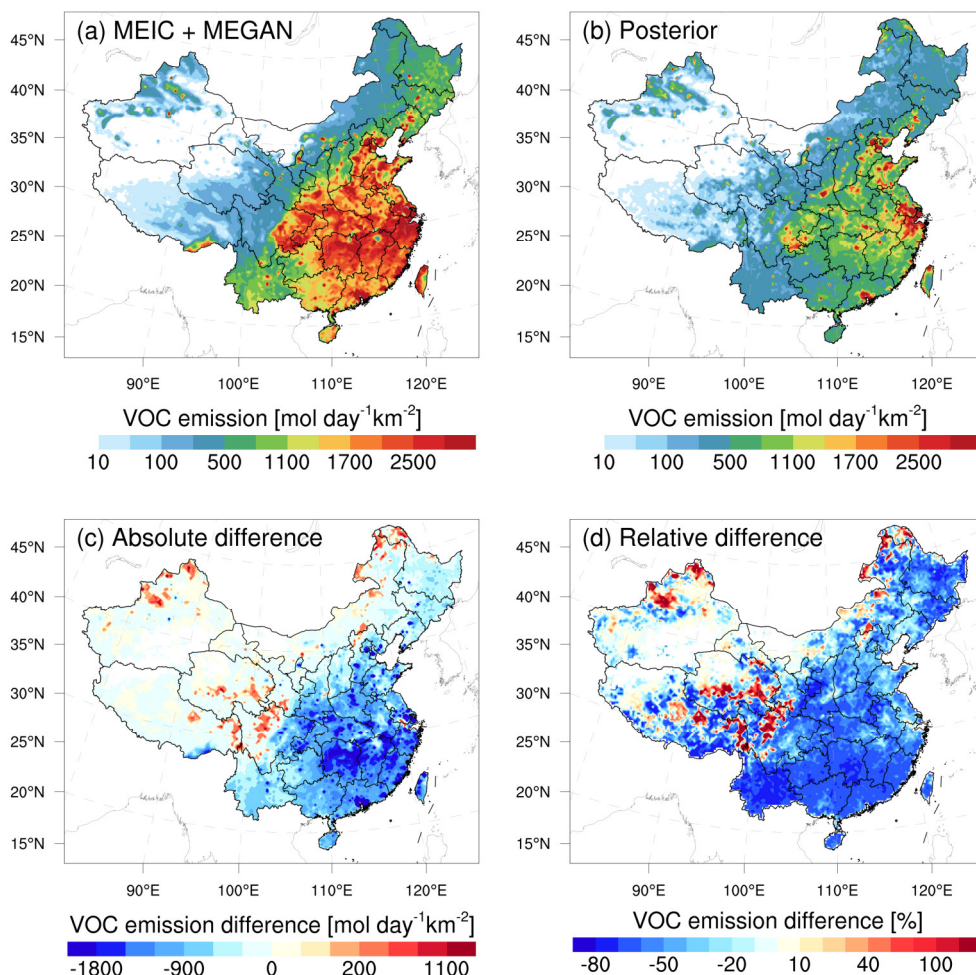
Figure 2. Spatial distribution of the time-averaged (a) prior emissions (MEIC 2020 + MEGAN), (b) posterior emissions, (c) absolute difference (posterior minus prior), and (d) relative difference of NMVOCs over China.

Table 2 shows the changes in emissions of biogenic NMVOCs across different land cover types (Figure S5) after inversion. The most significant reduction in biogenic emissions occurred within woody savannas, accounting for 26.9% of the overall reduction, followed by savannas and croplands, accounting for 21.2% and 17.2% respectively. Among all vegetation types, the broadleaf evergreen forests, recognized as the primary source of isoprene emission (Wang et al., 2021a), presented the greatest uncertainty, with NMVOC emissions experiencing a significant reduction of 66.2%. Standard emission rates in MEGAN are derived from leaf- or canopy-scale flux

measurements and extrapolated globally across regions sharing similar landcover characteristics, based on very limited observations (Guenther et al., 1995). This methodology introduces biases due to the large variability in emission rates among plant species.

Table 2. Prior and posterior biogenic NMVOC emissions, as well as their differences for different land cover types.

Land cover type	Prior Mmol/month	Posterior Mmol/month	Difference Mmol/month (%)
Evergreen needleleaf forests	955.7	549.3	-406.4 (-42.5)
Evergreen broadleaf forests	13985.1	4728.2	-9256.8 (-66.2)
Deciduous needleleaf forests	46.6	48.8	2.2 (4.7)
Deciduous broadleaf forests	8335.5	3487.4	-4848.1 (-58.2)
Mixed forests	8731.0	3961.7	-4769.4 (-54.6)
Closed shrublands	9.7	3.7	-6.0 (-61.5)
Open shrublands	21.3	8.6	-12.8 (-59.8)
Woody savannas	39327.2	16925.2	-22402.0 (-57.0)
Savannas	28319.7	10629.4	-17690.3 (-62.5)
Grasslands	16912.7	14269.6	-2643.1 (-15.6)
Permanent wetlands	286.1	115.4	-170.8 (-59.7)
Croplands	25537.8	11215.5	-14322.2 (-56.1)
Cropland-natural vegetation mosaics	10894.7	4289.8	-6605.0 (-60.6)
Sparsely vegetated	1814.7	1644.0	-170.6 (-9.4)

4.2 Evaluations for Posterior Emissions

The NO_x emissions were first evaluated by indirectly comparing the forward simulated NO_2 concentrations with measurements. As shown in Figure S6, the CEP with prior emissions exhibited positive biases in eastern China and negative biases in western China. However, when posterior emissions were used in the VEP, a substantial improvement in simulation performance was observed. Biases were limited to within ± 3 μg m^{-3}, and correlation coefficients exceeded 0.7 across the entire region. Figure 3 presents the simulated HCHO VCDs using prior and posterior NMVOCs emissions,

along with their associated biases. Both experiments showed high VCDs over central and eastern China, especially in the YRD and SCB. However, the CEP displayed substantial overestimation across most of mainland China, with the largest bias reaching 12×10^{15} molec cm^{-2} in Central China. Conversely, the VEP demonstrated notable improvements in both the magnitude and spatial distribution of simulated HCHO columns after the inversion compared to TROPOMI retrievals. More than 84% of the areas exhibited biases of less than 1×10^{15} molec cm^{-2}, and no significant spatial variation was observed. Overall, the biases in simulated HCHO VCDs decreased by 75.7% after the inversion. These results emphasize the efficiency of our system in reducing uncertainty in both NO$_x$ and NMVOC emissions.
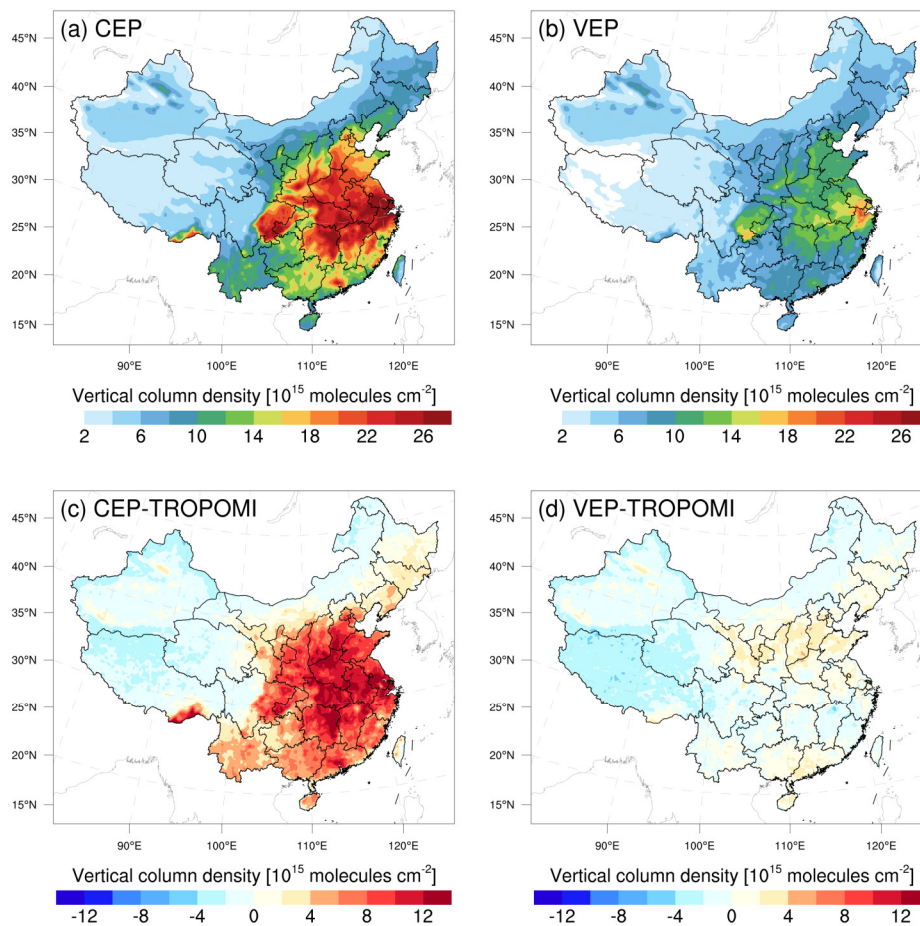
Figure 3. Simulated HCHO vertical column densities using prior (a) and posterior (b) NMVOC emissions, along with their biases (c and d) against TROPOMI measurement. All model results were sampled at TROPOMI overpass time.

4.3 Implications for Surface O$_3$

Figure 4 shows the spatial distribution of the mean bias (BIAS), root mean square error (RMSE), and correlation coefficient (CORR) for simulated O$_3$ concentrations in the CEP1 and VEP experiments compared to assimilated observations. Beyond the northwestern region of China, the CEP1 exhibited significant overestimation throughout the entire area, with a BIAS of 20.5 μg m^{-3}. In the VEP, the modeled O$_3$ chemical production were alleviated, especially in the southern regions of China where NMVOC emissions had significantly decreased. Overall, observation-constrained NMVOC emissions resulted in a 49.3% decrease in the BIAS, bringing it down to 10.4 μg m^{-3}. Additionally, the RMSE showed noticeable improvement due to the assimilation of HCHO observation, reducing the value from 30.9 to 23.3 μg m^{-3}. Despite a significant reduction in NMVOC emissions after inversion, notable overestimations persisted in northern provinces such as Liaoning, Hebei, Shanxi, and Shaanxi. This may be attributed to limited NMVOC constraints resulting from insufficient observations during the study period (Figures 1b and 3d). The remaining discrepancies between simulations and observations can be attributed to the combined results of intricate urban-rural sensitivity regimes and O$_3$ photochemistry reactions, which may not be comprehensively represented by CMAQ model, masking any potential improvement expected from the constrained emissions (See Sect. 4.4). The CORR was comparable between the CEP1 and VEP experiments, reflecting that the CMAQ model effectively simulated the temporal variation of O$_3$ concentrations. The biases at the independent sites were similar to those at the assimilated sites (Figure S7). In comparison to CEP1, the decreasing ratios in BIAS and RMSE in VEP were 46.7% and 23.4%, respectively.

447
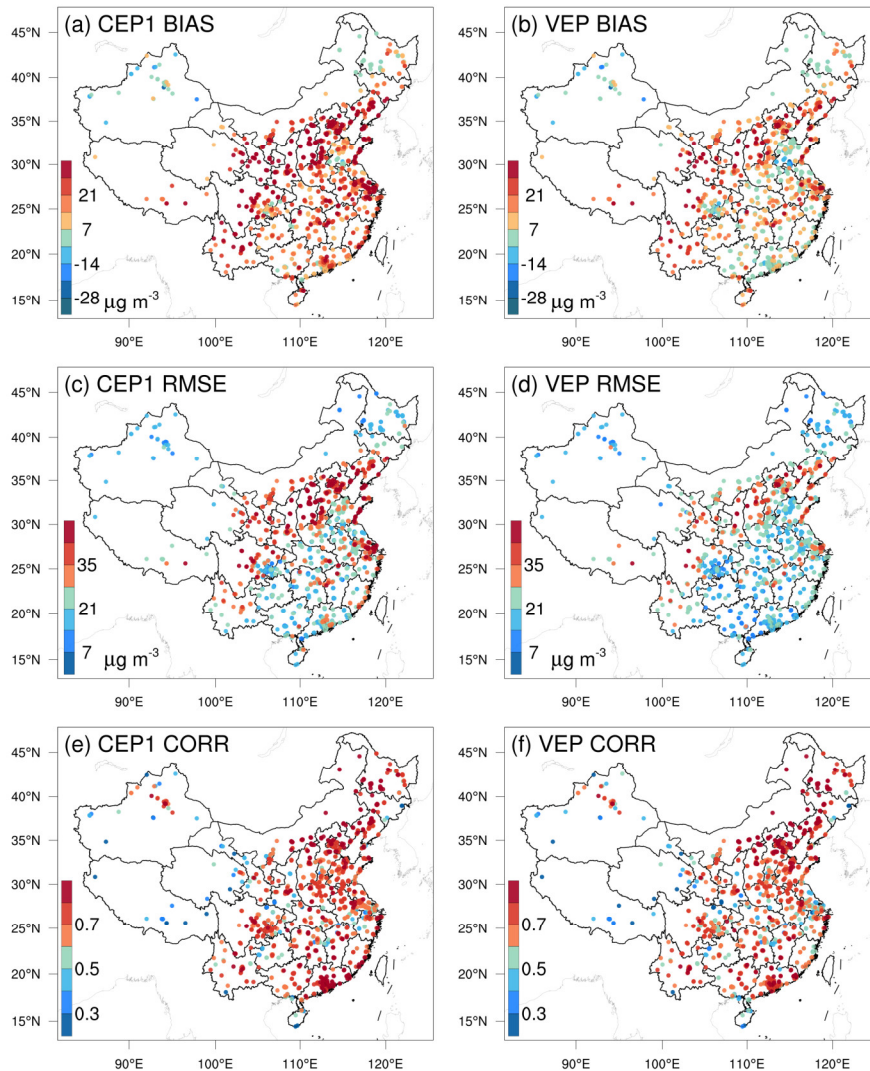
Figure 4. Spatial distribution of mean bias (BIAS, a and b), root mean square error (RMSE, c and d), and correlation coefficient (CORR, e and f) for simulated O_3 using prior (left, CEP1) and posterior (right, VEP) emissions, respectively, against assimilated observations.

Figure 5 shows the time series of simulated and observed hourly O_3 concentrations and their RMSEs, verified against surface monitoring sites. The VEP achieved better representations of diurnal O_3 variations compared with those in the CEP1, especially excelling in reproducing elevated O_3 concentrations at noon. Constraining the NMVOC emissions also led to better model simulations in terms of RMSE throughout the entire study period. Time-averaged BIAS and RMSE decreased from 20.6 and 37.3 $\mu g\ m^{-3}$ to 10.6 and 31.0 $\mu g\ m^{-3}$, respectively. We also evaluated the simulation results for seven key cities (i.e., Beijing, Shanghai, Guangzhou, Wuhan, Chongqing, Yinchuan, and Changchun, which represent key cities in North, East, South, Central, Southwest,

461 Northwest, and Northeast China, respectively), and the biases in the VEP with posterior

462 emissions all showed a significant reduction (Figure S8). Overall, the assimilation of

463 HCHO column observations effectively reduced NMVOC emission uncertainties and

464 consequently improved simulations of HCHO and O_3. These improvements hold

465 promise for further research into the implications of emission optimizations on regional

466 O_3 photochemistry.

467
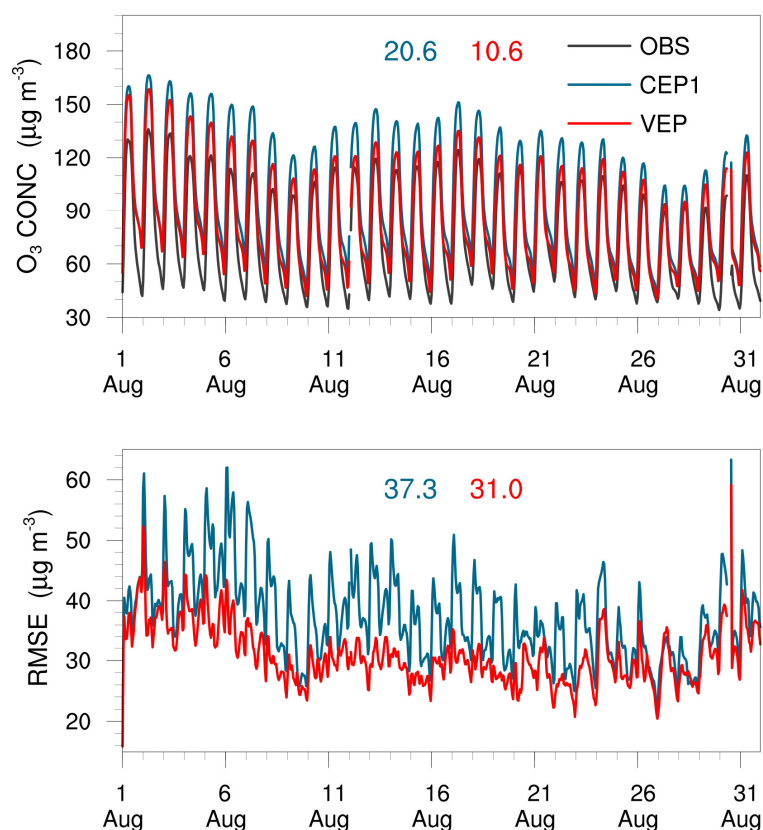
Figure 5. Time series comparison of hourly surface O_3 concentrations ($\mu g\ m^{-3}$) and

469 RMSE ($\mu g\ m^{-3}$) from CEP1 and VEP experiments against all observations at 1701

470 monitoring sites. The blue and red values on the graph represent the time-averaged

471 statistics in the CEP1 and VEP experiments, respectively.

472 As crucial O_3 precursors, the abundance of NMVOCs plays a significant role in

473 modulating O_3 production. Here we employed the IRRs to elucidate changes related to

474 O_3 production and loss at the surface, stemming from constrained NO_x and NMVOC

475 emissions. Figure 6 illustrates comparisons of the simulated maximum daily 8-hour

476 average (MDA8) surface O_3 levels and net reaction rates before and after the inversion.

477 The CEP1 exhibited an overestimation of O_3 levels, with a BIAS of 22.6% compared

478 to observed O_3 concentrations. This overestimation corresponded to the high net

479 chemical rates of O₃ in these areas (Figure S9). After inversion, O₃ net rates mitigated

480 in most regions. Consequently, the VEP experiment yielded results that closely aligned

481 with observations, with a BIAS of 9.2%. Referring to Figure 6e and 6f, differences in

482 production rates of O₃ closely track the changes in the NMVOC emissions (Figure 2).

483 The discrepancies in specific regions may be attributed to the complex nonlinear

484 relationships associated with O₃ and its precursors, which depend on prevailing

485 chemical regimes and regional transport. Additionally, changes in O₃ production

486 predominantly drive the overall decrease in O₃ concentrations, outweighing changes in

487 O₃ loss.
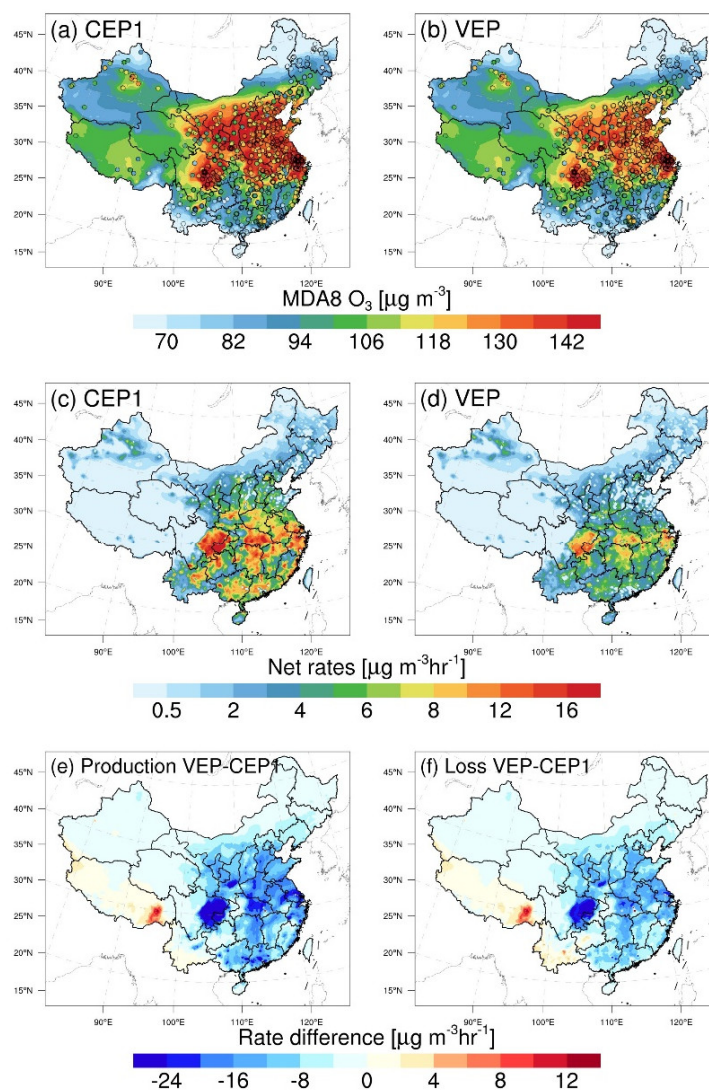
488

489 **Figure 6**. Comparisons of (a, b) simulated maximum daily 8-hour average (MDA8) O₃

490 concentrations, (c, d) net reaction rates, (e, f) and differences in production and loss

491 rates between CEP1 and VEP experiments at the surface. Surface MDA8 O₃ values

492 (circles) from the national control air quality stations were overlaid

493 Figure 7 shows the differences in the six principal pathways responsible for O_3 loss and
494 formation, when comparing simulations employing prior and posterior emissions. The
495 reactions of $HO_2 + NO$ and $RO_2 + NO$ are treated as the pathways leading to O_3
496 formation, whereas O_3 loss involves reactions including $NO2 + OH$, $O_3 + HO_2$, $O_3 +$
497 NMVOCs, and $O1D + H_2O$ (Wang et al., 2019). Our analysis was focused on the time
498 frame from 12:00 to 18:00 according to China standard time (CST). The differences
499 were computed by subtracting the simulation with posterior emissions from those with
500 prior emissions. Following the emission of NMVOCs, they undergo rapid oxidation by
501 atmospheric hydroxyl (OH) radicals. Due to the substantial decrease in NMVOC
502 emissions, there was a reduction in the production of hydroperoxy radicals (HO_2) and
503 organic peroxy radicals (RO_2) (Figure S10). Consequently, this reduction in HO_2/RO_2
504 levels, coupled with their reaction with NO, resulted in diminished O_3 production
505 (Figures 7a and 7b). A strong correlation was observed between changes in O_3
506 production via the $RO_2 + NO$ reaction and NMVOC emissions (Figure 2), consistent
507 with the findings of Souri et al. (2020). Typically, in NMVOC-rich environments, a
508 decrease in NMVOC emissions boosts OH concentrations. Consequently, we noted an
509 enhancement in the $NO_2 + OH$ reaction in the eastern and central regions of China. In
510 response to heightened HO_x concentrations over these areas, an increased O_3 loss
511 through the $O_3 + HO_x$ pathway was observed. Furthermore, we detected a substantial
512 decrease in O_3 loss through reactions with NMVOCs, especially in the southern China,
513 where substantial isoprene emissions are prevalent. This reduction was primarily
514 attributable to the decrease in NMVOC and O_3 levels. While the $NMVOC + O_3$ reaction
515 proceeds at a substantially slower rate $NMVOC + OH$, this specific chemical pathway
516 remains significant in oxidizing NMVOC and forming HO_x in forests areas (Paulson
517 and Orlando, 1996). The difference in $O1D + H_2O$ is primarily driven by the decrease
518 of O_3 photolysis. Although the rate of O_3 loss decreases in some chemical pathways,
519 overall, the rate of O_3 production dominates the changes in O_3 concentration.
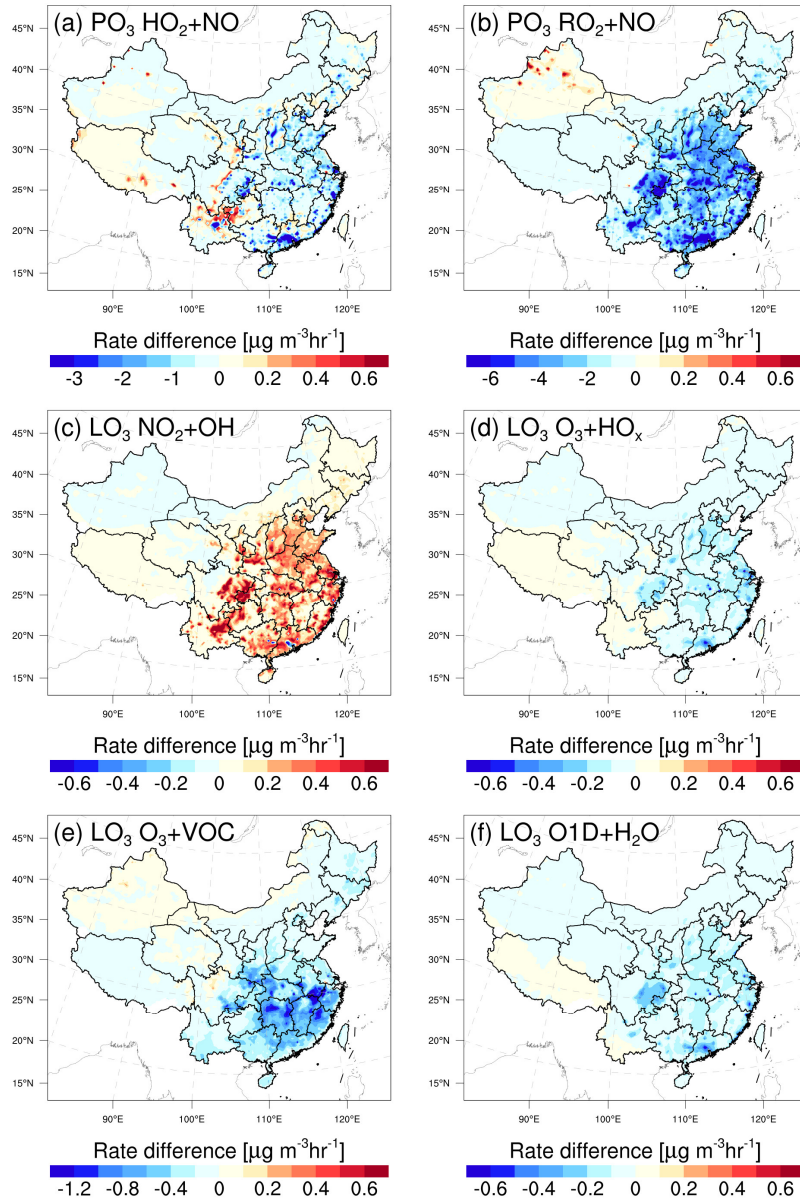
Figure 7. Differences in six major pathways of O_3 production and loss between CEP1 and VEP experiments at the surface. Time period: August 2022, 12:00–18:00 CST. PO_3 and LO_3 represent the pathways of O_3 formation and loss, respectively.

4.4 Discussions

O_3 simulations over China have a tendency to be overestimated in studies involving chemical transport modeling. For example, by intercomparing 14 state-of-the-art CTMs with O_3 observations within the framework of the MICS-Asia III, Li et al. (2019) identified a substantial overestimation of annual surface O_3 in East Asia, ranging from 20 to 60 µg m^{-3}. Notably, the NCP exhibited substantial overestimations, with most models overestimating O_3 by 100–200% during May–October. Despite our

optimization of O_3 precursor emissions, the posterior simulations still exhibit some degree of overestimation (Figure 4), suggesting that there may indeed be an effect of systematic bias, such as meteorological fields, spatial resolution, model treatments of nonlinear photochemistry and other physical processes. The WRF can generally reproduce meteorological conditions sufficiently in terms of their temporal variation and magnitude over China (Figure S11), with small biases of -0.5 °C, -5.3%, 0.3 m/s, and -42.4 m for temperature at 2 m, relative humidity at 2 m, and wind speed at 10 m, and planetary boundary layer height, respectively. However, due to the relatively coarse spatial resolution, NO titration effects in urban areas may not be well represented in the model, which can lead to an overestimation of O_3 in these areas. Additionally, model inherent errors arising from the model structure, parameterization, and the simplification or lack of chemical mechanisms inevitably affect the O_3 simulations. For example, Li et al. (2018) reported that heterogeneous reactions of nitrogen compounds could weaken the atmospheric oxidation capacity and thus reduce surface O_3 concentration by 20–40 $\mu g\ m^{-3}$ for the polluted regions over China. These reactions have not been fully incorporated in CMAQ chemical mechanisms. However, there is still a lack of reasonable and effective algorithms for addressing model errors through assimilation (Houtekamer and Zhang, 2016).O_3 concentration and NO_x (VOC) emissions are positively correlated in the NO_x (VOC)-limited region and negatively correlated in the VOC (NO_x)-limited region (Tang et al., 2011). Therefore, the uncertainty in NO_x emissions can affect the model's diagnosis of O_3-NO_x-VOC sensitivity, thereby introducing substantial model errors in the HCHO yield from VOC oxidation. In the base inversion experiment (EMDA), we simultaneously assimilated NO_2 and HCHO observations to optimize NO_x and NMVOC emissions. To evaluate the impact of optimized NO_x emissions on O_3-VOC chemistry, EMS disregarded the uncertainty of NO_x and focused on optimizing NMVOC emissions. Compared to the EMDA, in areas where NO_x is significantly overestimated, NMVOC emissions in the EMS have correspondingly decreased (Figure 8b). This might be due to under high-NO_x conditions, HCHO production occurs promptly, thereby compensating for the substantial amount of HCHO already present in the atmosphere by reducing emissions (Chan Miller et al., 2017). Figure S12 shows comparisons of concentrations and RMSE between the simulations using posterior emissions from EMS and EMDA experiments. Compared to VEP, CEP2 showed a larger RMSE, highlighting the necessity for simultaneous optimization of NO_x emissions when evaluating the impact of NMVOC

emission optimization on O_3. Additionally, CEP2 using prior NO_x emissions exhibited lower O_3 levels over parts of NCP and YRD, as well as some urban areas (Figure 8c), but with larger biases and RMSEs (Figure 8d). The reduction in NMVOC emissions contributed to a partial decrease in O_3 concentration. More significantly, these areas typically align with VOC-limited mechanisms (Wang et al., 2019; Wang et al., 2021c). Therefore, the overestimation of NO_x emissions (Figure S4) excessively inhibits O_3 accumulation due to the titration effect, thereby disrupting the evaluation of NMVOC contributions to O_3. This substantial disparity also seriously affects O_3 source apportionment, precursor-sensitive area delineation, and emissions reduction policy formulation.
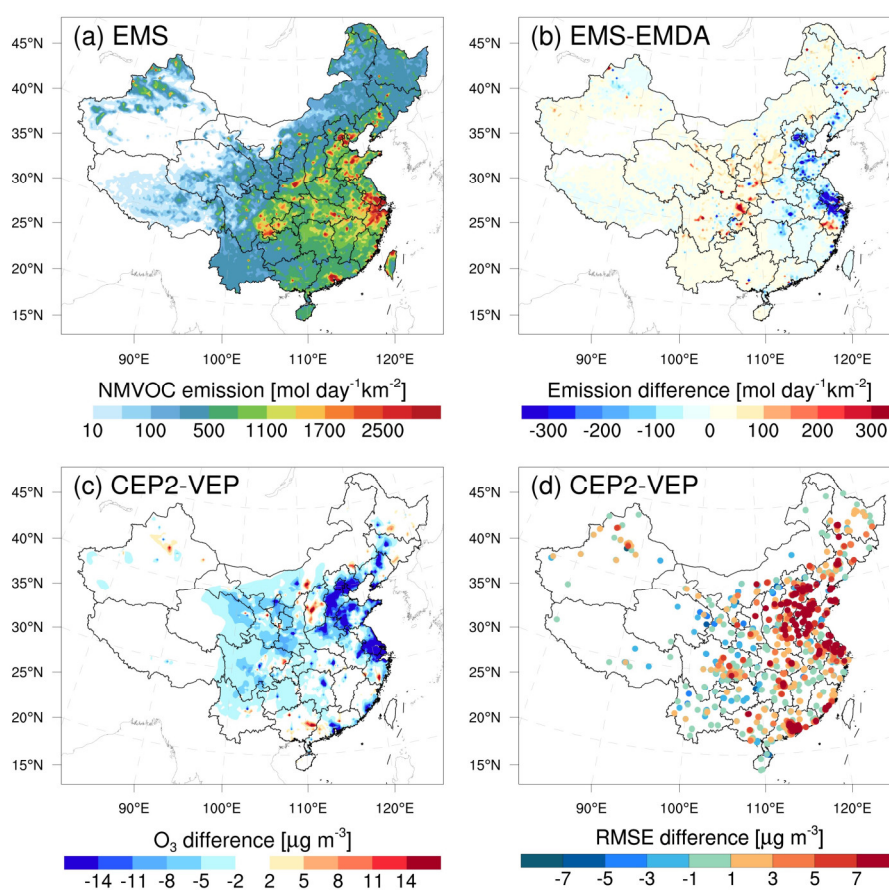
Figure 8. Spatial distribution of (a) posterior emissions in the EMS experiment, (b) differences in posterior emissions between EMS and EMDA, and differences in simulated (c) O_3 concentrations and (d) RMSE between CEP2 and VEP experiments. EMS did not optimize NO_x emissions compared to EMDA.

5 Summary and Conclusions

In this study, we extended the RAPAS assimilation system with the EnKF assimilation algorithm to optimize NMVOC emissions using the TROPOMI HCHO retrievals. Taking the MEIC 2020 for anthropogenic emissions and MEGANv2.1 output for biogenic sources as a priori, NMVOC emissions over China in August 2022 were inferred. Importantly, we implicitly took the chemical feedback among VOC-NO_x-O_3 into account by simultaneously adjusting NO_x emissions using nationwide in-situ NO_2 observations. Furthermore, we quantified the impact of NMVOC emission inversion on surface O_3 pollution using the CMAQ-IRR model.

The application of TROPOMI HCHO observations as constraints led to a substantial reduction of 50.2% compared to the prior emissions for NMVOCs in August 2022. A domain-wide significant decrease was found over central and southern China with abundant forests, especially for the broadleaf evergreen forests, implying a considerable overestimation of biogenic NMVOC emissions. Observation-constrained emissions significantly improved the performance of surface NO_2 and HCHO column simulations, reducing biases by 97.4% and 75.7%, respectively. This highlights the effectiveness of the RAPAS in reducing uncertainty in NO_x and NMVOC emissions. Isolating the impact of NO_x emission changes, the posterior NMVOC emissions significantly mitigated the overestimation in prior O_3 simulations, resulting in a 49.3% decrease in surface O_3 biases. This is mainly attributed to a substantial decrease in the RO2 + NO reaction rate (a major pathway for O_3 production) and an increase NO_2 + OH reaction rate (a major pathway for O_3 loss) during the afternoon, resulting in a decrease in the simulated MDA8 surface O_3 concentrations by approximately 15 $\mu g\ m^{-3}$.

Sensitivity inversions demonstrate the robustness of top-down emissions to variations in prior uncertainty settings, yet they are sensitive to HCHO column biases, highlighting the importance of comprehensive validation studies utilizing available remote-sensing data and, if possible, airborne validation campaigns. Moreover, we found that, in comparison to optimizing NMVOC emissions alone, the joint optimization of NMVOC and NO_x emissions can significantly improve the overall performance of O_3 simulations. Ignoring errors in NO_x emissions introduces uncertainty in quantifying the impact of NMVOC emissions on surface O_3, especially in areas where overestimated NO_x emissions can unrealistically amplify titration effects,

613 highlighting the necessity of simultaneous optimization of NO_x emissions.

614

Data availability

616 The observations used for assimilation and the optimized emissions in this study can be

617 accessed at https://doi.org/10.5281/zenodo.10079006 (Feng and Jiang, 2023).

618

Author contribution

620 SF and FJ conceived and designed the research. SF developed the data assimilation

621 code, analyzed data, and prepared the paper with contributions from all co-authors. FJ

622 supervised and assisted in conceptualization and writing. TQ, NW, MJ, SZ, JC, FY, and

623 WJ reviewed and commented on the paper.

624

Competing interests

626 The authors declare that they have no conflict of interest.

627

Acknowledgements

629 This work is supported by the National Key R&D Program of China (Grant No.

630 2022YFB3904801), the National Natural Science Foundation of China (Grant No:

631 42305116 and 42377102), the Natural Science Foundation of Jiangsu Province of China

632 (Grant No: BK20230801), and the Hangzhou Agricultural and Social Development

633 Scientific Research Project (Grant No: 202203B29). The authors also gratefully

634 acknowledge the High-Performance Computing Center (HPCC) of Nanjing University

635 for doing the numerical calculations in this paper on its blade cluster system.

636

References

638 Angot, H., McErlean, K., Hu, L., Millet, D. B., Hueber, J., Cui, K., Moss, J., Wielgasz, C., Milligan,
639   T., Ketcherside, D., Bret-Harte, M. S., and Helmig, D.: Biogenic volatile organic compound
640   ambient mixing ratios and emission rates in the Alaskan Arctic tundra, Biogeosciences, 17,
641   6219-6236, 10.5194/bg-17-6219-2020, 2020.

642 Bauwens, M., Stavrakou, T., Müller, J. F., De Smedt, I., Van Roozendael, M., van der Werf, G. R.,
643   Wiedinmyer, C., Kaiser, J. W., Sindelarova, K., and Guenther, A.: Nine years of global
644   hydrocarbon emissions based on source inversion of OMI formaldehyde observations, Atmos.
645   Chem. Phys., 16, 10133-10158, 10.5194/acp-16-10133-2016, 2016.

Byun, D., and Schere, K. L.: Review of the governing equations, computational algorithms, and other components of the models-3 Community Multiscale Air Quality (CMAQ) modeling system, Applied Mechanics Reviews, 59, 51-77, 10.1115/1.2128636, 2006.

Cao, H., Fu, T. M., Zhang, L., Henze, D. K., Miller, C. C., Lerot, C., Abad, G. G., De Smedt, I., Zhang, Q., van Roozendael, M., Hendrick, F., Chance, K., Li, J., Zheng, J., and Zhao, Y.: Adjoint inversion of Chinese non-methane volatile organic compound emissions using space-based observations of formaldehyde and glyoxal, Atmos. Chem. Phys., 18, 15017-15046, 10.5194/acp-18-15017-2018, 2018.

Chaliyakunnel, S., Millet, D. B., and Chen, X.: Constraining Emissions of Volatile Organic Compounds Over the Indian Subcontinent Using Space-Based Formaldehyde Measurements, Journal of Geophysical Research: Atmospheres, 124, 10525-10545, 10.1029/2019JD031262, 2019.

Chan Miller, C., Jacob, D. J., Marais, E. A., Yu, K., Travis, K. R., Kim, P. S., Fisher, J. A., Zhu, L., Wolfe, G. M., Hanisco, T. F., Keutsch, F. N., Kaiser, J., Min, K. E., Brown, S. S., Washenfelder, R. A., González Abad, G., and Chance, K.: Glyoxal yield from isoprene oxidation and relation to formaldehyde: chemical mechanism, constraints from SENEX aircraft observations, and interpretation of OMI satellite data, Atmos. Chem. Phys., 17, 8725-8738, 10.5194/acp-17-8725-2017, 2017.

Cheng, S., Cheng, X., Ma, J., Xu, X., Zhang, W., Lv, J., Bai, G., Chen, B., Ma, S., Ziegler, S., Donner, S., and Wagner, T.: Mobile MAX-DOAS observations of tropospheric NO2 and HCHO during summer over the Three Rivers' Source region in China, Atmos. Chem. Phys., 23, 3655-3677, 10.5194/acp-23-3655-2023, 2023.

Curci, G., Palmer, P. I., Kurosu, T. P., Chance, K., and Visconti, G.: Estimating European volatile organic compound emissions using satellite observations of formaldehyde from the Ozone Monitoring Instrument, Atmos. Chem. Phys., 10, 11501-11517, 10.5194/acp-10-11501-2010, 2010.

De Smedt, I., Theys, N., Yu, H., Danckaert, T., Lerot, C., Compernolle, S., Van Roozendael, M., Richter, A., Hilboll, A., Peters, E., Pedergnana, M., Loyola, D., Beirle, S., Wagner, T., Eskes, H., van Geffen, J., Boersma, K. F., and Veefkind, P.: Algorithm theoretical baseline for formaldehyde retrievals from S5P TROPOMI and from the QA4ECV project, Atmos. Meas. Tech., 11, 2395-2426, 10.5194/amt-11-2395-2018, 2018.

Elbern, H., Strunk, A., Schmidt, H., and Talagrand, O.: Emission rate and chemical state estimation by 4-dimensional variational inversion, Atmospheric Chemistry and Physics, 7, 3749-3769, 10.5194/acp-7-3749-2007, 2007.

Fang, X., Shao, M., Stohl, A., Zhang, Q., Zheng, J., Guo, H., Wang, C., Wang, M., Ou, J., Thompson, R. L., and Prinn, R. G.: Top-down estimates of benzene and toluene emissions in the Pearl River Delta and Hong Kong, China, Atmos. Chem. Phys., 16, 3369-3382, 10.5194/acp-16-3369-2016, 2016.

Feng, S., Jiang, F., Jiang, Z., Wang, H., Cai, Z., and Zhang, L.: Impact of 3DVAR assimilation of surface PM2.5 observations on PM2.5 forecasts over China during wintertime, Atmospheric Environment, 187, 34-49, 10.1016/j.atmosenv.2018.05.049, 2018.

Feng, S., Jiang, F., Wang, H., Wang, H., Ju, W., Shen, Y., Zheng, Y., Wu, Z., and Ding, A.: NOx Emission Changes Over China During the COVID-19 Epidemic Inferred From Surface NO2 Observations, Geophysical Research Letters, 47, 10.1029/2020gl090080, 2020.

Feng, S., Jiang, F., Wang, H., Shen, Y., Zheng, Y., Zhang, L., Lou, C., and Ju, W.: Anthropogenic emissions estimated using surface observations and their impacts on PM2.5 source apportionment over the Yangtze River Delta, China, Science of The Total Environment, 828, 154522, 10.1016/j.scitotenv.2022.154522, 2022.

Feng, S., Jiang, F., Wu, Z., Wang, H., He, W., Shen, Y., Zhang, L., Zheng, Y., Lou, C., Jiang, Z., and Ju, W.: A Regional multi-Air Pollutant Assimilation System (RAPAS v1.0) for emission estimates: system development and application, Geosci. Model Dev., 16, 5949-5977, 10.5194/gmd-16-5949-2023, 2023.

Gaspari, G., and Cohn, S. E.: Construction of correlation functions in two and three dimensions, Quarterly Journal of the Royal Meteorological Society, 125, 723-757, 10.1256/smsqj.55416, 1999.

Guenther, A. B., Jiang, X., Heald, C. L., Sakulyanontvittaya, T., Duhl, T., Emmons, L. K., and Wang, X.: The Model of Emissions of Gases and Aerosols from Nature version 2.1 (MEGAN2.1): an extended and updated framework for modeling biogenic emissions, Geoscientific Model Development, 5, 1471-1492, 10.5194/gmd-5-1471-2012, 2012.

Hong, C., Zhang, Q., He, K., Guan, D., Li, M., Liu, F., and Zheng, B.: Variations of China's emission estimates: response to uncertainties in energy statistics, Atmos. Chem. Phys., 17, 1227-1239, 10.5194/acp-17-1227-2017, 2017.

Hong, Q., Liu, C., Hu, Q., Zhang, Y., Xing, C., Su, W., Ji, X., and Xiao, S.: Evaluating the feasibility of formaldehyde derived from hyperspectral remote sensing as a proxy for volatile organic compounds, Atmospheric Research, 264, 105777, 10.1016/j.atmosres.2021.105777, 2021.

Houtekamer, P. L., and Zhang, F.: Review of the Ensemble Kalman Filter for Atmospheric Data Assimilation, Monthly Weather Review, 144, 4489-4532, 10.1175/mwr-d-15-0440.1, 2016.

Jiang, X., Guenther, A., Potosnak, M., Geron, C., Seco, R., Karl, T., Kim, S., Gu, L., and Pallardy, S.: Isoprene emission response to drought and the impact on global atmospheric chemistry, Atmospheric Environment, 183, 69-83, 10.1016/j.atmosenv.2018.01.026, 2018.

Kaiser, J., Jacob, D. J., Zhu, L., Travis, K. R., Fisher, J. A., González Abad, G., Zhang, L., Zhang, X., Fried, A., Crounse, J. D., St. Clair, J. M., and Wisthaler, A.: High-resolution inversion of OMI formaldehyde columns to quantify isoprene emission on ecosystem-relevant scales: application to the southeast US, Atmos. Chem. Phys., 18, 5483-5497, 10.5194/acp-18-5483-2018, 2018.

Li, B., Ho, S. S. H., Li, X., Guo, L., Chen, A., Hu, L., Yang, Y., Chen, D., Lin, A., and Fang, X.: A comprehensive review on anthropogenic volatile organic compounds (VOCs) emission estimates in China: Comparison and outlook, Environment International, 156, 106710, 10.1016/j.envint.2021.106710, 2021.

Li, J., Chen, X., Wang, Z., Du, H., Yang, W., Sun, Y., Hu, B., Li, J., Wang, W., Wang, T., Fu, P., and Huang, H.: Radiative and heterogeneous chemical effects of aerosols on ozone and inorganic aerosols over East Asia, Science of The Total Environment, 622-623, 1327-1342, 10.1016/j.scitotenv.2017.12.041, 2018.

Li, J., Nagashima, T., Kong, L., Ge, B., Yamaji, K., Fu, J. S., Wang, X., Fan, Q., Itahashi, S., Lee, H. J., Kim, C. H., Lin, C. Y., Zhang, M., Tao, Z., Kajino, M., Liao, H., Li, M., Woo, J. H., Kurokawa, J., Wang, Z., Wu, Q., Akimoto, H., Carmichael, G. R., and Wang, Z.: Model evaluation and intercomparison of surface-level ozone and relevant species in East Asia in the

context of MICS-Asia Phase III – Part 1: Overview, Atmos. Chem. Phys., 19, 12993-13015, 10.5194/acp-19-12993-2019, 2019.

Li, K., Jacob, D. J., Shen, L., Lu, X., De Smedt, I., and Liao, H.: Increases in surface ozone pollution in China from 2013 to 2019: anthropogenic and meteorological influences, Atmos. Chem. Phys., 20, 11423-11433, 10.5194/acp-20-11423-2020, 2020.

Li, M., Liu, H., Geng, G., Hong, C., Liu, F., Song, Y., Tong, D., Zheng, B., Cui, H., Man, H., Zhang, Q., and He, K.: Anthropogenic emission inventories in China: a review, National Science Review, 4, 834-866, 10.1093/nsr/nwx150, 2017a.

Li, M., Zhang, Q., Kurokawa, J.-i., Woo, J.-H., He, K., Lu, Z., Ohara, T., Song, Y., Streets, D. G., Carmichael, G. R., Cheng, Y., Hong, C., Huo, H., Jiang, X., Kang, S., Liu, F., Su, H., and Zheng, B.: MIX: a mosaic Asian anthropogenic emission inventory under the international collaboration framework of the MICS-Asia and HTAP, Atmospheric Chemistry And Physics, 17, 935-963, 10.5194/acp-17-935-2017, 2017b.

Liu, H., Liu, Z., and Lu, F.: A Systematic Comparison of Particle Filter and EnKF in Assimilating Time-Averaged Observations, Journal of Geophysical Research-Atmospheres, 122, 13155-13173, 10.1002/2017jd026798, 2017.

Liu, Z., Wang, Y., Vrekoussis, M., Richter, A., Wittrock, F., Burrows, J. P., Shao, M., Chang, C.-C., Liu, S.-C., Wang, H., and Chen, C.: Exploring the missing source of glyoxal (CHOCHO) over China, Geophysical Research Letters, 39, 10.1029/2012GL051645, 2012.

Marais, E. A., Jacob, D. J., Guenther, A., Chance, K., Kurosu, T. P., Murphy, J. G., Reeves, C. E., and Pye, H. O. T.: Improved model of isoprene emissions in Africa using Ozone Monitoring Instrument (OMI) satellite observations of formaldehyde: implications for oxidants and particulate matter, Atmos. Chem. Phys., 14, 7693-7703, 10.5194/acp-14-7693-2014, 2014.

Marsh, D. R., Mills, M. J., Kinnison, D. E., Lamarque, J.-F., Calvo, N., and Polvani, L. M.: Climate Change from 1850 to 2005 Simulated in CESM1(WACCM), Journal of Climate, 26, 7372-7391, 10.1175/JCLI-D-12-00558.1, 2013.

Mo, Z., Huang, S., Yuan, B., Pei, C., Song, Q., Qi, J., Wang, M., Wang, B., Wang, C., Li, M., Zhang, Q., and Shao, M.: Deriving emission fluxes of volatile organic compounds from tower observation in the Pearl River Delta, China, Science of The Total Environment, 741, 139763, 10.1016/j.scitotenv.2020.139763, 2020.

Mu, M., Randerson, J. T., van der Werf, G. R., Giglio, L., Kasibhatla, P., Morton, D., Collatz, G. J., DeFries, R. S., Hyer, E. J., Prins, E. M., Griffith, D. W. T., Wunch, D., Toon, G. C., Sherlock, V., and Wennberg, P. O.: Daily and 3-hourly variability in global fire emissions and consequences for atmospheric model predictions of carbon monoxide, Journal of Geophysical Research-Atmospheres, 116, 10.1029/2011jd016245, 2011.

Opacka, B., Müller, J.-F., Stavrakou, T., Miralles, D. G., Koppa, A., Pagán, B. R., Potosnak, M. J., Seco, R., De Smedt, I., and Guenther, A. B.: Impact of Drought on Isoprene Fluxes Assessed Using Field Data, Satellite-Based GLEAM Soil Moisture and HCHO Observations from OMI, Remote Sensing, 14, 2021, 2022.

Palmer, P. I., Abbot, D. S., Fu, T.-M., Jacob, D. J., Chance, K., Kurosu, T. P., Guenther, A., Wiedinmyer, C., Stanton, J. C., Pilling, M. J., Pressley, S. N., Lamb, B., and Sumner, A. L.: Quantifying the seasonal and interannual variability of North American isoprene emissions using satellite observations of the formaldehyde column, Journal of Geophysical Research:

Atmospheres, 111, 10.1029/2005JD006689, 2006.

Paulson, S. E., and Orlando, J. J.: The reactions of ozone with alkenes: An important source of HOx in the boundary layer, Geophysical Research Letters, 23, 3727-3730, 10.1029/96GL03477, 1996.

Pierce, T., Geron, C., Bender, L., Dennis, R., Tonnesen, G., and Guenther, A.: Influence of increased isoprene emissions on regional ozone modeling, Journal of Geophysical Research: Atmospheres, 103, 25611-25629, 10.1029/98JD01804, 1998.

Ren, J., Guo, F., and Xie, S.: Diagnosing ozone–NOx–VOC sensitivity and revealing causes of ozone increases in China based on 2013–2021 satellite retrievals, Atmos. Chem. Phys., 22, 15035-15047, 10.5194/acp-22-15035-2022, 2022.

Seco, R., Holst, T., Davie-Martin, C. L., Simin, T., Guenther, A., Pirk, N., Rinne, J., and Rinnan, R.: Strong isoprene emission response to temperature in tundra vegetation, Proceedings of the National Academy of Sciences, 119, e2118014119, doi:10.1073/pnas.2118014119, 2022.

Skamarock, W. C., and Klemp, J. B.: A time-split nonhydrostatic atmospheric model for weather research and forecasting applications, Journal Of Computational Physics, 227, 3465-3485, 10.1016/j.jcp.2007.01.037, 2008.

Souri, A. H., Nowlan, C. R., González Abad, G., Zhu, L., Blake, D. R., Fried, A., Weinheimer, A. J., Wisthaler, A., Woo, J. H., Zhang, Q., Chan Miller, C. E., Liu, X., and Chance, K.: An inversion of NOx and non-methane volatile organic compound (NMVOC) emissions using satellite observations during the KORUS-AQ campaign and implications for surface ozone over East Asia, Atmos. Chem. Phys., 20, 9837-9854, 10.5194/acp-20-9837-2020, 2020.

Souri, A. H., Chance, K., Bak, J., Nowlan, C. R., González Abad, G., Jung, Y., Wong, D. C., Mao, J., and Liu, X.: Unraveling pathways of elevated ozone induced by the 2020 lockdown in Europe by an observationally constrained regional model using TROPOMI, Atmos. Chem. Phys., 21, 18227-18245, 10.5194/acp-21-18227-2021, 2021.

Su, W., Liu, C., Chan, K. L., Hu, Q., Liu, H., Ji, X., Zhu, Y., Liu, T., Zhang, C., Chen, Y., and Liu, J.: An improved TROPOMI tropospheric HCHO retrieval over China, Atmos. Meas. Tech., 13, 6271-6292, 10.5194/amt-13-6271-2020, 2020.

Tang, X., Zhu, J., Wang, Z. F., and Gbaguidi, A.: Improvement of ozone forecast over Beijing based on ensemble Kalman filter with simultaneous adjustment of initial conditions and emissions, Atmospheric Chemistry And Physics, 11, 12901-12916, 10.5194/acp-11-12901-2011, 2011.

van der Werf, G. R., Randerson, J. T., Giglio, L., van Leeuwen, T. T., Chen, Y., Rogers, B. M., Mu, M., van Marle, M. J. E., Morton, D. C., Collatz, G. J., Yokelson, R. J., and Kasibhatla, P. S.: Global fire emissions estimates during 1997-2016, Earth System Science Data, 9, 697-720, 10.5194/essd-9-697-2017, 2017.

Vigouroux, C., Langerock, B., Bauer Aquino, C. A., Blumenstock, T., Cheng, Z., De Mazière, M., De Smedt, I., Grutter, M., Hannigan, J. W., Jones, N., Kivi, R., Loyola, D., Lutsch, E., Mahieu, E., Makarova, M., Metzger, J. M., Morino, I., Murata, I., Nagahama, T., Notholt, J., Ortega, I., Palm, M., Pinardi, G., Röhling, A., Smale, D., Stremme, W., Strong, K., Sussmann, R., Té, Y., van Roozendael, M., Wang, P., and Winkler, H.: TROPOMI–Sentinel-5 Precursor formaldehyde validation using an extensive network of ground-based Fourier-transform infrared stations, Atmos. Meas. Tech., 13, 3751-3767, 10.5194/amt-13-3751-2020, 2020.

Wang, H., Lu, X., Seco, R., Stavrakou, T., Karl, T., Jiang, X., Gu, L., and Guenther, A. B.: Modeling

Isoprene Emission Response to Drought and Heatwaves Within MEGAN Using Evapotranspiration Data and by Coupling With the Community Land Model, Journal of Advances in Modeling Earth Systems, 14, e2022MS003174, 10.1029/2022MS003174, 2022.

Wang, H., Yan, R., Xu, T., Wang, Y., Wang, Q., Zhang, T., An, J., Huang, C., Gao, Y., Gao, Y., Li, X., Yu, C., Jing, S., Qiao, L., Lou, S., Tao, S., and Li, Y.: Observation Constrained Aromatic Emissions in Shanghai, China, Journal of Geophysical Research: Atmospheres, 125, e2019JD031815, 10.1029/2019JD031815, 2020.

Wang, H., Wu, Q., Guenther, A. B., Yang, X., Wang, L., Xiao, T., Li, J., Feng, J., Xu, Q., and Cheng, H.: A long-term estimation of biogenic volatile organic compound (BVOC) emission in China from 2001–2016: the roles of land cover change and climate variability, Atmos. Chem. Phys., 21, 4825-4848, 10.5194/acp-21-4825-2021, 2021a.

Wang, J., Yan, R., Wu, G., Liu, Y., Wang, M., Zeng, N., Jiang, F., Wang, H., He, W., Wu, M., Ju, W., and Chen, J. M.: Unprecedented decline in photosynthesis caused by summer 2022 record-breaking compound drought-heatwave over Yangtze River Basin, Science Bulletin, 68, 2160-2163, 10.1016/j.scib.2023.08.011, 2023.

Wang, N., Lyu, X., Deng, X., Huang, X., Jiang, F., and Ding, A.: Aggravating O3 pollution due to NOx emission control in eastern China, Science of The Total Environment, 677, 732-744, 10.1016/j.scitotenv.2019.04.388, 2019.

Wang, P., Liu, Y., Dai, J., Fu, X., Wang, X., Guenther, A., and Wang, T.: Isoprene Emissions Response to Drought and the Impacts on Ozone and SOA in China, Journal of Geophysical Research: Atmospheres, 126, e2020JD033263, 10.1029/2020JD033263, 2021b.

Wang, W., van der A, R., Ding, J., van Weele, M., and Cheng, T.: Spatial and temporal changes of the ozone sensitivity in China based on satellite and ground-based observations, Atmos. Chem. Phys., 21, 7253-7269, 10.5194/acp-21-7253-2021, 2021c.

Warneke, C., de Gouw, J. A., Del Negro, L., Brioude, J., McKeen, S., Stark, H., Kuster, W. C., Goldan, P. D., Trainer, M., Fehsenfeld, F. C., Wiedinmyer, C., Guenther, A. B., Hansel, A., Wisthaler, A., Atlas, E., Holloway, J. S., Ryerson, T. B., Peischl, J., Huey, L. G., and Hanks, A. T. C.: Biogenic emission measurement and inventories determination of biogenic emissions in the eastern United States and Texas and comparison with biogenic emission inventories, Journal of Geophysical Research: Atmospheres, 115, 10.1029/2009JD012445, 2010.

Whitaker, J. S., and Hamill, T. M.: Ensemble data assimilation without perturbed observations, Monthly Weather Review, 130, 1913-1924, 10.1175/1520-0493(2002)130<1913:Edawpo>2.0.Co;2, 2002.

Wolfe, G. M., Kaiser, J., Hanisco, T. F., Keutsch, F. N., de Gouw, J. A., Gilman, J. B., Graus, M., Hatch, C. D., Holloway, J., Horowitz, L. W., Lee, B. H., Lerner, B. M., Lopez-Hilifiker, F., Mao, J., Marvin, M. R., Peischl, J., Pollack, I. B., Roberts, J. M., Ryerson, T. B., Thornton, J. A., Veres, P. R., and Warneke, C.: Formaldehyde production from isoprene oxidation across NOx regimes, Atmos. Chem. Phys., 16, 2597-2610, 10.5194/acp-16-2597-2016, 2016.

Yuan, B., Kaser, L., Karl, T., Graus, M., Peischl, J., Campos, T. L., Shertz, S., Apel, E. C., Hornbrook, R. S., Hills, A., Gilman, J. B., Lerner, B. M., Warneke, C., Flocke, F. M., Ryerson, T. B., Guenther, A. B., and de Gouw, J. A.: Airborne flux measurements of methane and volatile organic compounds over the Haynesville and Marcellus shale gas production regions, Journal of Geophysical Research: Atmospheres, 120, 6271-6289, 10.1002/2015JD023242, 2015.

Zhang, M., Zhao, C., Yang, Y., Du, Q., Shen, Y., Lin, S., Gu, D., Su, W., and Liu, C.: Modeling sensitivities of BVOCs to different versions of MEGAN emission schemes in WRF-Chem (v3.6) and its impacts over eastern China, Geosci. Model Dev., 14, 6155-6175, 10.5194/gmd-14-6155-2021, 2021.

Zhang, Q., Streets, D. G., Carmichael, G. R., He, K. B., Huo, H., Kannari, A., Klimont, Z., Park, I. S., Reddy, S., Fu, J. S., Chen, D., Duan, L., Lei, Y., Wang, L. T., and Yao, Z. L.: Asian emissions in 2006 for the NASA INTEX-B mission, Atmos. Chem. Phys., 9, 5131-5153, 10.5194/acp-9-5131-2009, 2009.

Zheng, B., Tong, D., Li, M., Liu, F., Hong, C., Geng, G., Li, H., Li, X., Peng, L., Qi, J., Yan, L., Zhang, Y., Zhao, H., Zheng, Y., He, K., and Zhang, Q.: Trends in China's anthropogenic emissions since 2010 as the consequence of clean air actions, Atmospheric Chemistry And Physics, 18, 14095-14111, 10.5194/acp-18-14095-2018, 2018.

Zhou, B., Guo, H., Zeren, Y., Wang, Y., Lyu, X., Wang, B., and Wang, H.: An Observational Constraint of VOC Emissions for Air Quality Modeling Study in the Pearl River Delta Region, Journal of Geophysical Research: Atmospheres, 128, e2022JD038122, 10.1029/2022JD038122, 2023.